J Therm Spray Tech
https://doi.org/10.1007/s11666-026-02204-7

ORIGINAL RESEARCH ARTICLE

Mechanical and Fracture Properties of As-Built Inconel 718 Produced by High-Speed Laser Directed Energy Deposition: Stability to Process Parameters Variation

Ondrej Kovarik[1] · Simone Maffia[2] · Tobias Stittgen[2] · Filip Wick[3,4] · Vojtech Lukes[3,4] · Abhinav Anand[3,5] · Jan Cizek[3,4]

Submitted: 31 August 2025 / in revised form: 31 January 2026 / Accepted: 26 February 2026

Abstract Directed energy deposition (DED) is a group of efficient additive manufacturing methods for creating complex-shaped components. Of these, the next-generation high-speed laser-based directed energy deposition (HS DED-LB) combines high-speed kinematics and a high-power infrared laser, offering unparalleled deposition speeds. Due to its novelty, the mechanical and fracture properties of the HS DED-LB deposits are virtually unknown. In this pioneer study, a series of unique testing methods was used to determine the properties and assess the influence of the inherent microstructure. As a model material, Inconel 718 was selected as an industrially relevant superalloy. To demonstrate the HS DED-LB capabilities, it was printed at a high powder feed rate of 30 g/min at different levels of laser power (up to 2400 W) and scanning speeds (up to 60 m/min). The corresponding linear energy densities ranged from 1.8 to 3.6 kJ/m, i.e., values significantly higher than those of powder bed fusion methods and lower than those of conventional DED. The method was shown to be very robust as, in this range, the tested mechanical and fracture properties differed by less than 10%. The HS DED-LB Inconel 718 exhibited a specific microstructure and texture, owing to the inherent thermal history of the melt pool. This is a favorable material state, similar to that of the traditional directionally solidified Inconel superalloys used in aerospace.

Keywords additive manufacturing · fatigue crack growth rate · fracture toughness · high-speed directed energy deposition · Ni superalloy · stress–strain · texture

This article is an invited paper selected from presentations at the 2025 International Thermal Spray Conference, held May 5–8, 2025, in Vancouver, Canada, and has been expanded from the original presentation. The issue was organized by Giovanni Bolelli, University of Modena and Reggio Emilia (Lead Editor); Fardad Azarmi, North Dakota State University; Sara Bagherifard, Politecnico di Milano; Partha Pratim Bandyopadhyay, Indian Institute of Technology, Kharagpur; Šárka Houdková, University of West Bohemia; Heli Koivuluoto, Tampere University; Yuk-Chiu Lau, General Electric Power (Retired); Hua Li, Ningbo Institute of Materials Technology and Engineering, CAS; Sinan Müftü, Northeastern University; and Filofteia-Laura Toma, Fraunhofer Institute for Material and Beam Technology.

✉ Ondrej Kovarik
ondrej.kovarik@fjfi.cvut.cz

[1] Faculty of Nuclear Sciences and Physical Engineering, Czech Technical University in Prague, Prague, Czech Republic

[2] Ponticon GmbH, Wiesbaden, Germany

[3] Institute of Plasma Physics of the Czech Academy of Sciences, Prague, Czech Republic

[4] Department of Materials Engineering, Faculty of Mechanical Engineering, Czech Technical University, Prague, Czech Republic

[5] Politecnico di Milano, Milan, Italy

Introduction

Inconel 718 is a γ' and γ''-strengthened Nb-containing Ni superalloy employed in extremely high-temperature applications in aerospace and power generation (Ref 1). Due to the slow precipitation of the strengthening phases, the alloy is weldable with a reduced affinity for solidification cracking. As such, its fabrication by additive manufacturing (AM) methods is relatively straight-forward. Different deposition technologies, such as cold spray (CS (Ref 2)), laser beam powder bed fusion (PBF-LB (Ref 3-5)), and laser-based directed energy deposition (DED-LB (Ref 6-10)), have already been used for Inconel 718 deposition.

Published online: 26 March 2026

Of these, the methods involving localized material melting, i.e., PBF-LB and DED-LB, offer a flexible way of tailoring the deposit microstructure, as shown both experimentally (Ref 11, 12) and numerically (Ref 13). As a result of steep thermal gradients and a relatively low solidification rate, the Ni-based superalloys deposited by these two techniques often exhibit a favorable directional solidification (Ref 12, 14). Consequently, in the as-built condition, the microstructure comprises elongated columnar fibers grouped into coherent clusters. While such microstructure exhibits a texture and anisotropy similar to single crystals, it also contains structural interfaces parallel to the solidification direction: cell boundaries between individual fibers and grain boundaries between the clusters (Ref 15). Such microstructure combines the attractive properties of single crystals, such as creep, fatigue, and thermal shock resistances, with the good strength, toughness, and corrosion resistance of polycrystalline materials especially when loaded in the fiber direction (Ref 16). To subsequently increase its strength, solutionizing/aging treatment can be used to precipitation harden the printed Inconel 718 alloy. However, to preserve the favorable fiber microstructure, the heat treatment needs to be performed at sufficiently low solutionizing temperatures (Ref 17-19).

During the printing process of Inconel 718 as well as other superalloys prepared by PBF-LB and DED-LB, two main issues can arise, potentially decreasing the quality of the as-built material. Both are related to the material cooling rates and the linear energy density parameter η. As summarized in the review paper by Cavalcante et al. (Ref 12), η is related to two process parameters, laser power P and scanning speed v:

$$\eta = \frac{P}{v} \quad \text{(Eq 1)}$$

At too low cooling rates, i.e., high η, Laves phases can form through segregation of heavy elements, triggering detrimental effects such as limited ductility, stress concentration, and crack formation (Ref 12). Further, at very high η, turbulence can form in the melting pool of the overheated fluid, resulting in significant porosity of the material. At too high cooling rates, i.e., low η, solidification cracking may occur between the molten pool tracks, as observed for DED-LB Inconel 718 (Ref 20) or Inconel 738LC (Ref 21).

A precise control of the deposit parameters P and v is therefore necessary. The exact process window of the η parameter is not clearly defined, and mixed recommendations can be obtained from the existing literature (Ref 12).

The laser beam high-speed directed energy deposition process (Ref 22) was performed using the 3DMD technology developed by Ponticon GmbH (see Fig. 1). The 3DMD technology represents a unique combination of a high-power laser head coupled with a fast linear workpiece positioning stage, providing unprecedented productivity, precision, and material flexibility for industrial-scale employment. The technology is capable of deposition at very high scanning speeds, characterized by η as low as 1.8 kJ/m (Ref 23). This value is an order of magnitude lower than the $\eta \sim$ 20-250 kJ/m indicated for typical DED-LB processes (Ref 8-10) and, at the same time, one order of magnitude higher than $\eta \sim$ 0.1-1 kJ/m typical for PBF-LB processes (Ref 4, 5). To the best of our knowledge, there is no experimental study describing DED-LB materials produced at such η range. Consequently, the properties of such materials are unknown. This paper aims to investigate the missing information by testing Inconel 718 material deposited using the novel HS DED-LB method. Specifically, the study focuses on the simultaneous determination of the mechanical and fracture properties, including fracture toughness and fatigue crack growth rate. To reach the goal, two critical parameters, laser power P and laser head scanning speed v, were changed over a deliberately wide range, corresponding to a linear energy density from 1.8 to 3.6 kJ/m. A conventionally manufactured Inconel 718 material was tested as a reference.

The obtained results were then compared to the results of other AM methods obtained from the literature. Lastly, the methodology allowed for assessing the HS DED-LB process stability.

Experimental

Sample Preparation

Nine Inconel 718 blocks with approximate dimensions $50 \times 10 \times 9$ mm^3 were deposited on a 10 mm thick 1.0045 structural steel substrate (Fig. 2). Gas atomized Inconel 718 powder manufactured by Oerlikon Metco Inc. (Westbury, USA) with a granulometry of 15-45 µm was used as the feedstock material. The feedstock powder was used directly from factory-sealed bottles stored under inert gas, and no additional drying or conditioning was carried out.

The deposition was performed using a pE3D system (Ponticon GmbH, Wiesbaden, Germany) presented in Fig. 1. It is a HS DED-LB system offering linear speed up to 200 m/min with 50 m/s^2 acceleration. The system is equipped with a high-power diode laser source (Laserline GmbH, Mülheim Kärlich, DE) providing a maximum output power of 8400 W. The laser is coupled with a zoom optics module from the same manufacturer, with variable focal length and the circular top-hat spot diameters from 1.1 to 3.5 mm at the focal plane. The focal plane of the laser was set at 1 mm above the substrate surface. The

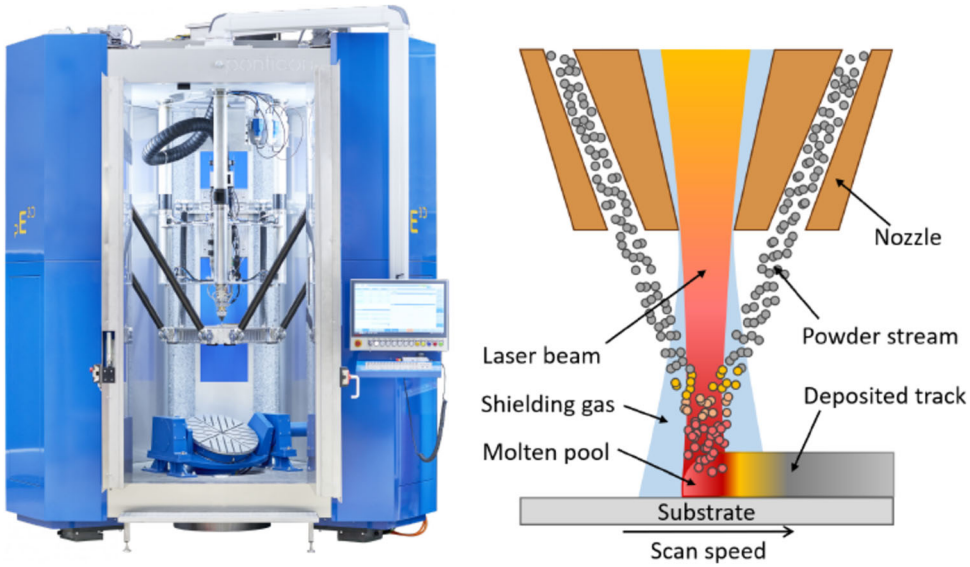

Fig. 1 pE3D HS DED-LB system and the schematic drawing of its deposition principle

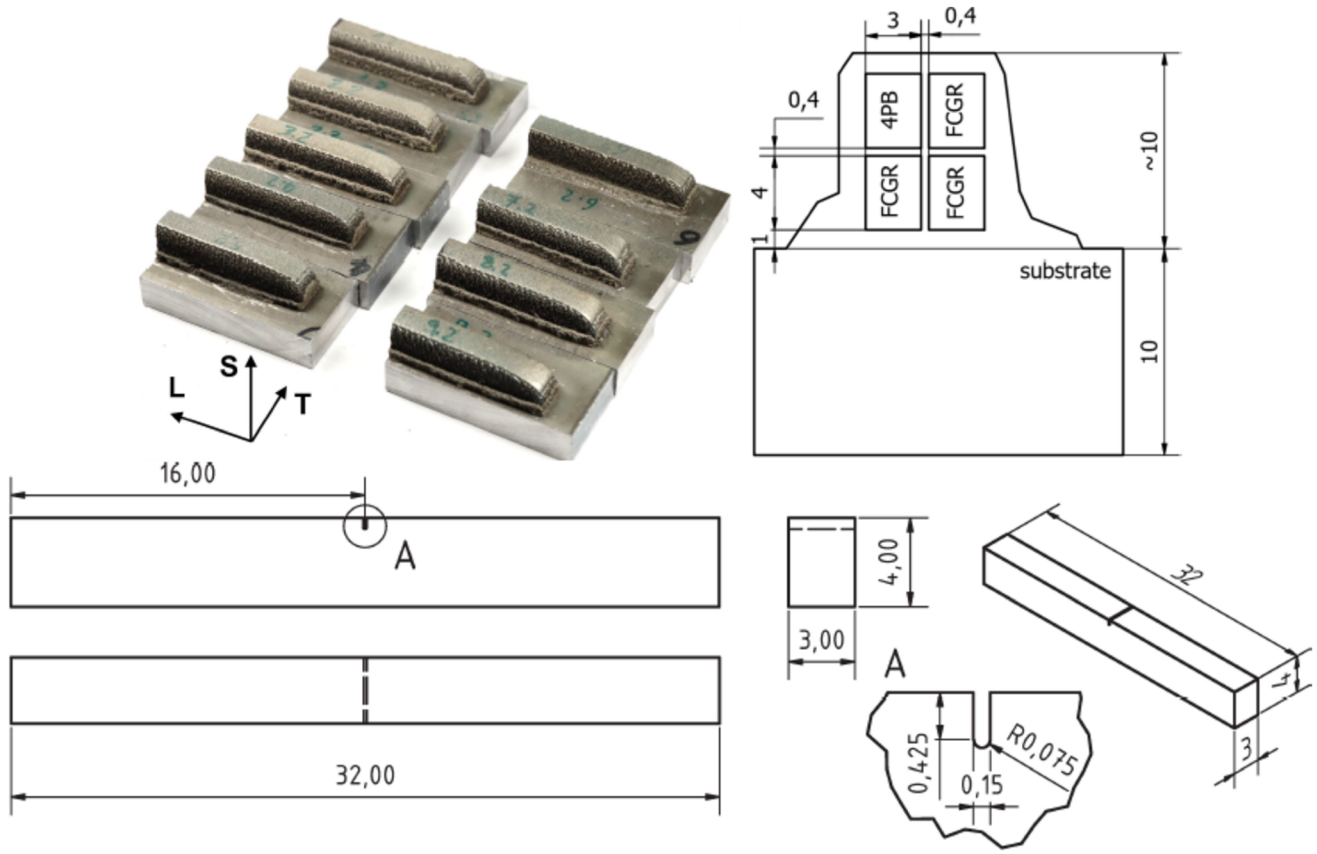

Fig. 2 Geometry of the deposited Inconel 718 blocks, a schematic drawing of their cutting plan, and a drawing of the universal specimens with a detail of the notch geometry

powder was delivered through a Coax40 coaxial ring nozzle (Fraunhofer ILT, Aachen, DE), focused to the same distance. To ensure adequate protection of the melt pool during the deposition, argon was used as shielding gas at a flow rate of 8 l/min. A simple meander pattern was used for the deposition, defining the coordinate system used in this study, with L and T representing the long and short meander directions, respectively, and S corresponding to the build direction (Fig. 2). No heat treatment of the material was performed after the printing. The tested

combinations of deposition parameters, i.e., laser power P and laser head scanning speed v are presented in Table 1. The specimen nomenclature P xvy used throughout this paper describes the laser power (x = 1800, 2100, 2400 W) and the scanning speed (y = 40, 50, 60 m/min). The scanning speeds used in this study were two orders of magnitude higher than the DED-LB parameters used by Bambach et al. (Ref 6), where the deposition occurred at a laser power of 1 kW and a scanning speed of 0.3 m/min, i.e., at η = 200 kJ/m. Additionally, the powder mass flow of 30 g/min (1.8 kg/h) in our study was an order of magnitude higher. In this regard, the HS DED-LB deposition process reached the build speed necessary for industrial-scale production of larger components such as combustion chambers or rocket engine nozzles.

Table 1 Process parameters used for HS DED-LB deposition of Inconel 718

Parameters	Values
Laser power P	1.8, 2.1, 2.4 kW
Scanning speed v	40, 50, 60 m/min
Laser spot size	1.2 mm
Raster spacing	0.6 mm
Powder feed rate	30 g/min
Shield Ar	8 l/min

The dimensions of the prepared deposits allowed the extraction of four 32 × 4 × 3 mm^3 specimens (Fig. 2) using electric discharge machining (EDM). All four specimens were oriented in the L-S direction according to the ASTM E399 nomenclature (Ref 24). Three of these specimens were then notched in the middle to a depth of 0.5 mm (Fig. 2) using a thin diamond blade, while the remaining fourth specimen was left unnotched.

A conventionally manufactured, wrought Inconel 718 in the form of a 12 mm thick bar (Bibus Metals AG, Fehraltorf, Switzerland) was used as a reference. The material was subjected to standard heat treatment comprising five steps: solution annealing at 1000 °C for 30 min in a protective atmosphere, quenching in water, two-step aging at 720 °C for 8 h, and 620 °C for 18 h, followed by air cooling to room temperature.

Characterization

The microstructure was observed using an SEM (JSM-IT500HR, JEOL, Tokyo, Japan) in electron channeling contrast mode (ECCI) using specimen cross sections polished by standard techniques and finished by vibratory polishing (Vibromet, Buehler, Lake Bluff, USA) in

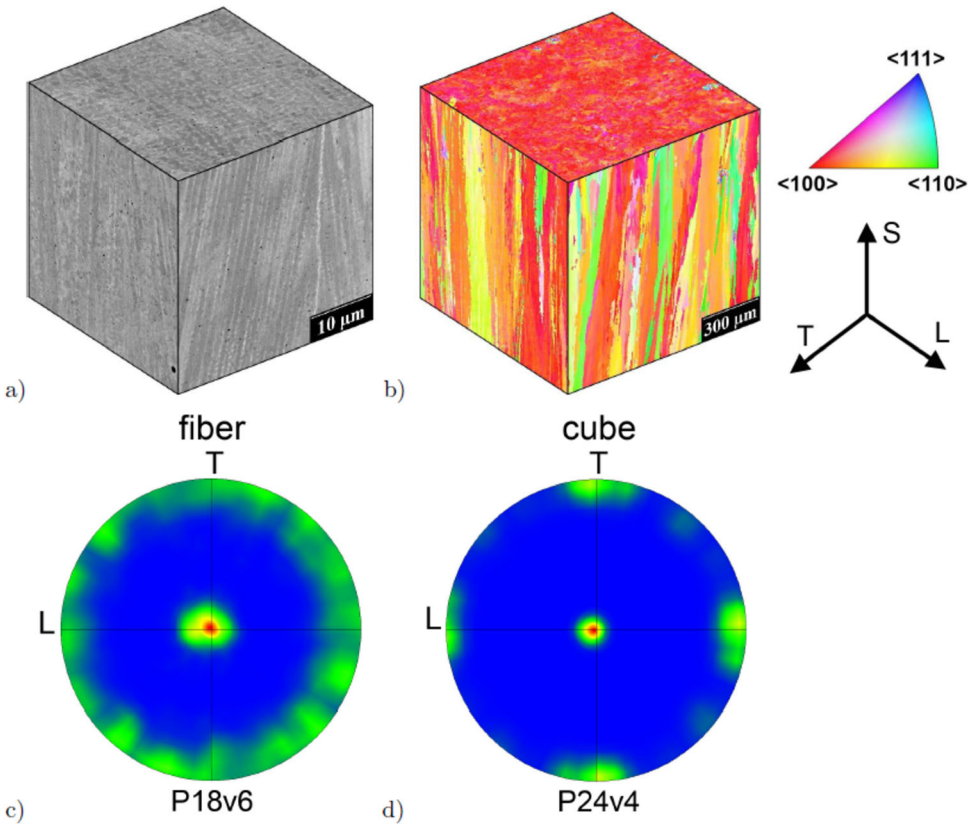

Fig. 3 A typical microstructure of the HS DED-LB Inconel 718 (P24v4 specimen shown) imaged by SEM ECCI contrast (a) and EBSD inverse pole figure (b). Pole figures of specimens with fiber (c) and cube textures (d)

colloidal silica for 8 hours. Detailed EBSD analyses were performed using the Velocity camera (EDAX LLC, Pleasanton, USA) and OIM software. The same SEM was used to investigate the fracture surfaces of the specimens after the fatigue crack growth rate and fracture toughness tests. The density of the deposits was measured using the Archimedes method, with two specimens per deposition condition. The porosity was further assessed by image analysis of the SEM cross section images (ImageJ, NIH, USA).

Stress–Strain Properties

Stress–strain properties were measured using the unnotched specimens, assuming symmetric tension–compression behavior. A procedure described in (Ref 25) using a four-point bending setup with the outer and inner supports span of 27 mm and 13.5 mm, respectively, was used. The central 6 mm of the specimen length was instrumented with a DIC system (a telecentric lens and the Ncorr DIC software (Ref 26)) to obtain the displacement field. The observed face was polished and etched in 2% H_2SO_4 electrolyte at 3 V for 5 s. The stress–strain curves were then extracted from the bending test data following the method of Herbert (Ref 27). The extracted curves were then processed to calculate the respective elastic moduli E and yield strengths YS.

Fracture Properties

The fatigue crack growth rates (FCGR) were measured using an own developed test device in resonance pure bending at a remote stress ratio $R \sim -1$ using the notched specimens. The resonance effect was used for bending stress excitation, as well as for precise measurement of the crack length (Ref 28). The rate control mode allowed to adjust the loading amplitude so that a prescribed crack growth rate $\frac{da}{dN}(a)$ was reached (Ref 29). Following the ASTM E647 (Ref 30) recommendation for negative remote stress ratios, it was assumed that $\Delta K = K_{\max}$.

The fracture toughness K_{IC} was measured in a three-point bend setup with an outer span of 27 mm according to the ASTM E1820 standard (Ref 31). For this measurement, specimens after the FCGR tests with crack lengths of approximately 2 mm were used. The crack extension was measured from the specimen compliance obtained by a displacement sensor.

Results and Discussion

Microstructure

A typical microstructure of the HS DED-LB Inconel 718 deposit is presented in Fig. 3(a). It comprises primary fibers

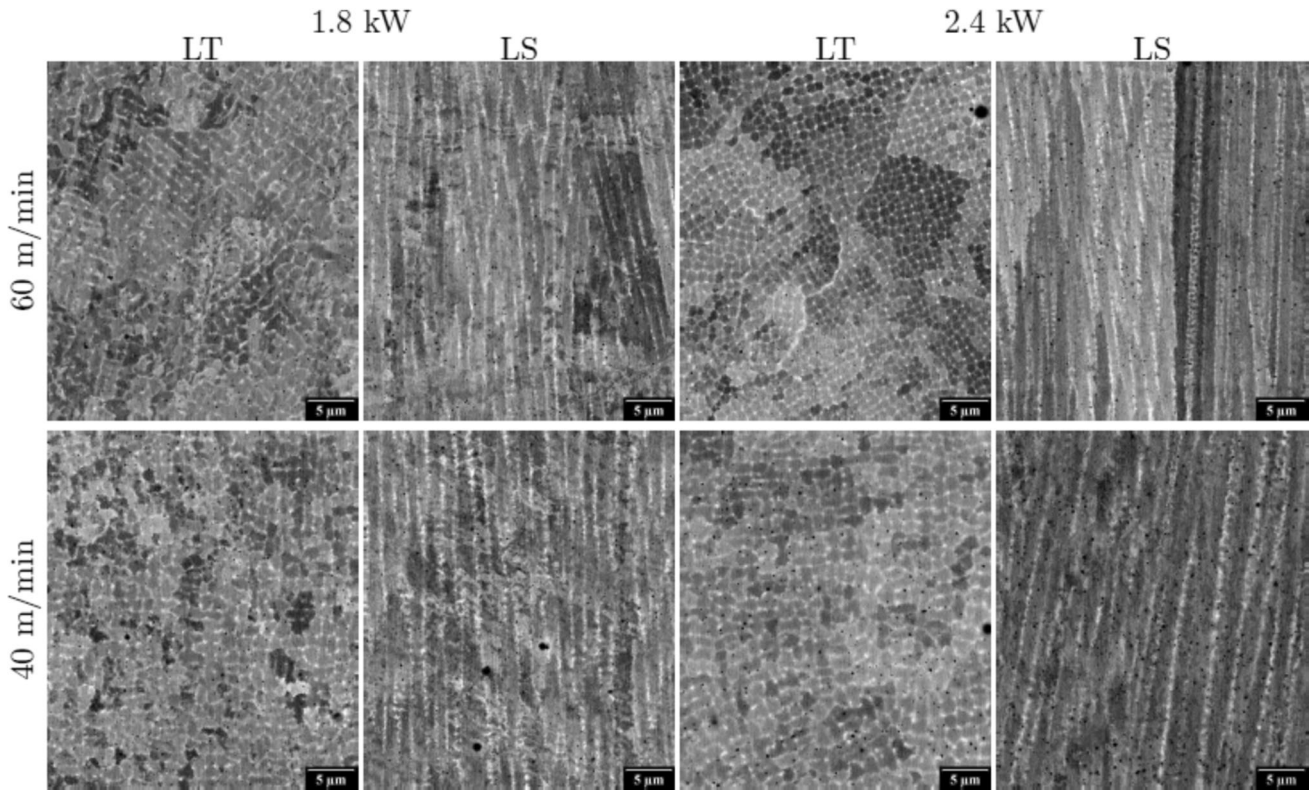

Fig. 4 Effect of process parameters on the deposit microstructure (SEM, ECCI contrast). The cross sections are shown in the LT and LS planes

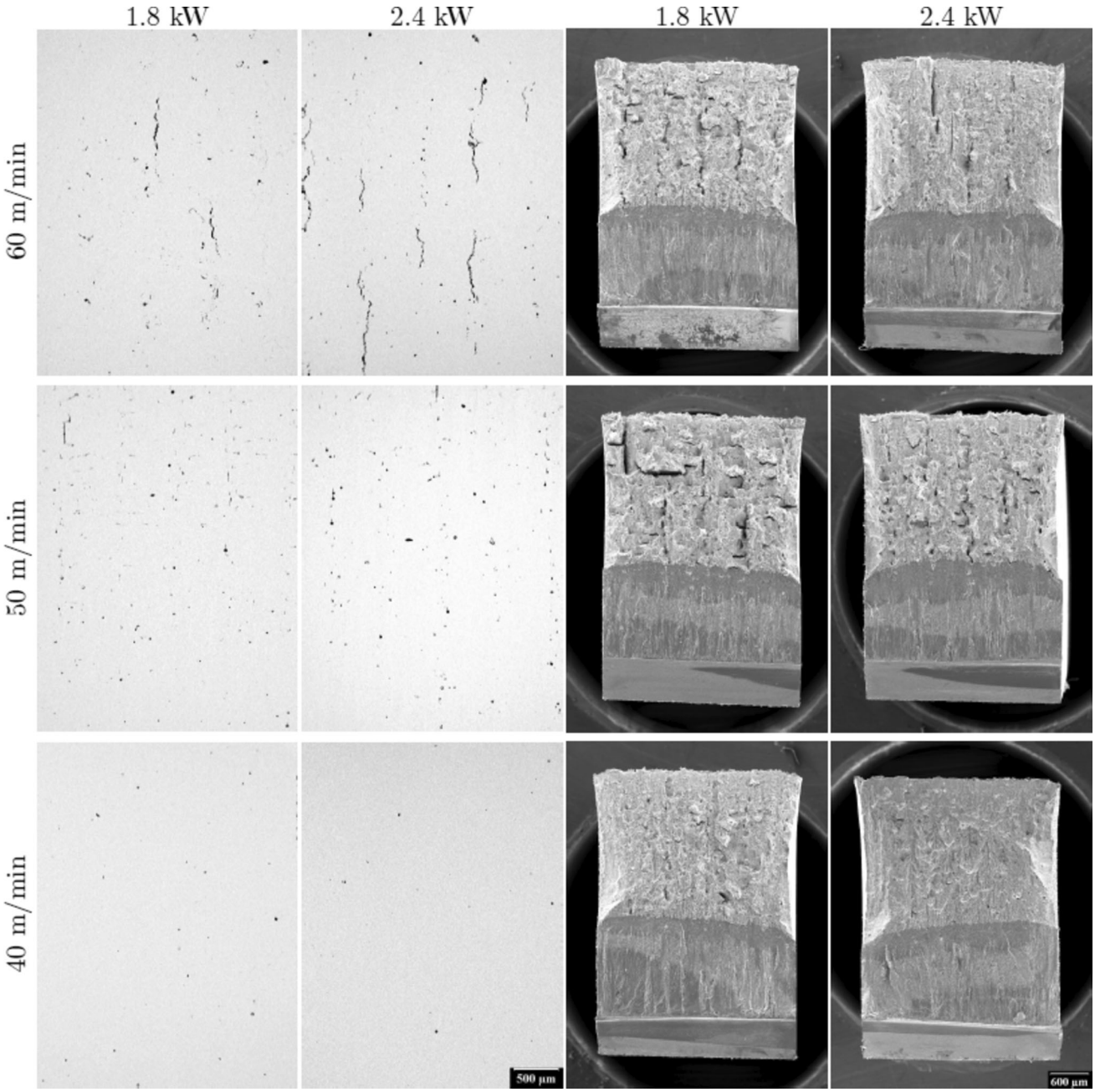

Fig. 5 Effect of process parameters on microstructure (SEM, BSE) and fracture surface (SEM, SE). The cross sections and fracture surfaces are shown in the TL and TS planes, respectively

separated by coherent Nb-rich cell boundaries, with several adjacent fibers sharing the same crystal orientation (Fig. 3b). According to (Ref 32), such a microstructure is typical for materials produced by fusion-based AM techniques and is formed by a combination of two mechanisms: epitaxial and equiaxial solidification. The major mechanism is the epitaxial growth, triggering the formation of the fibers. At higher v, the epitaxial mechanism is combined with the equiaxial solidification, triggering the formation of a fiber texture (Fig. 3c) with the [100] direction aligned to the S (build) direction. At a lower v, the equiaxial mechanism is not triggered, resulting in a cube texture (Fig. 3d) with the $<100>$ directions aligned to the L, T, and S directions. A similar fiber texture was observed in most Inconel alloys processed by DED-LB (Ref 21, 33), while the cube texture observed in our material was rarely reported.

The primary fiber microstructure was relatively similar for all nine tested process parameters, as illustrated in Fig. 4. The fiber size was slightly larger for lower scanning

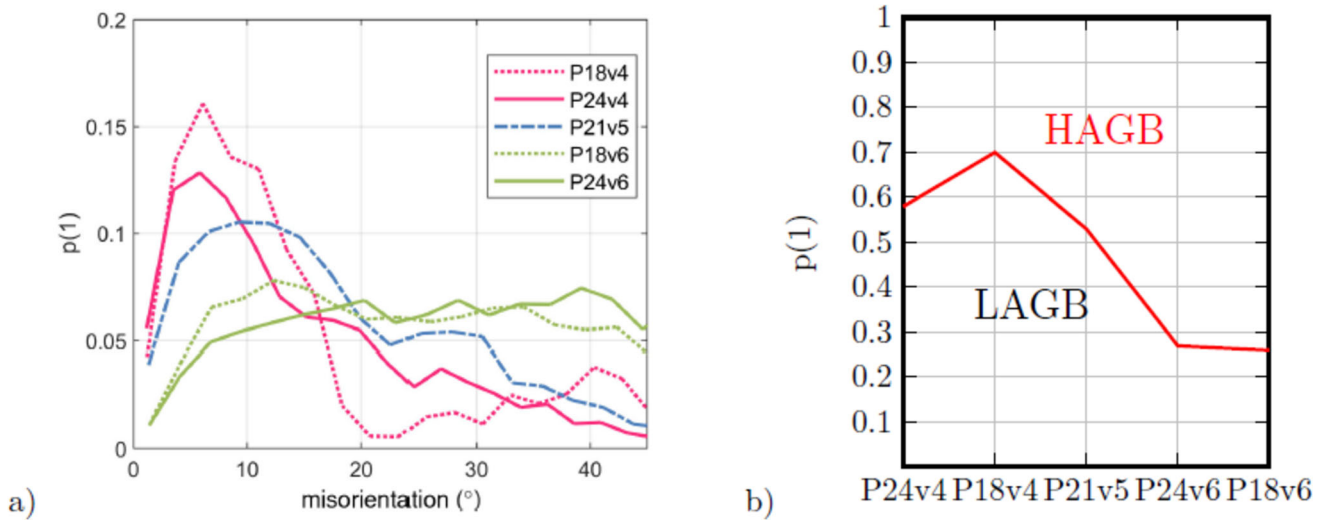

Fig. 6 Histogram of grain boundary misorientation (a) and the corresponding low-angle to high-angle boundary ratio (b)

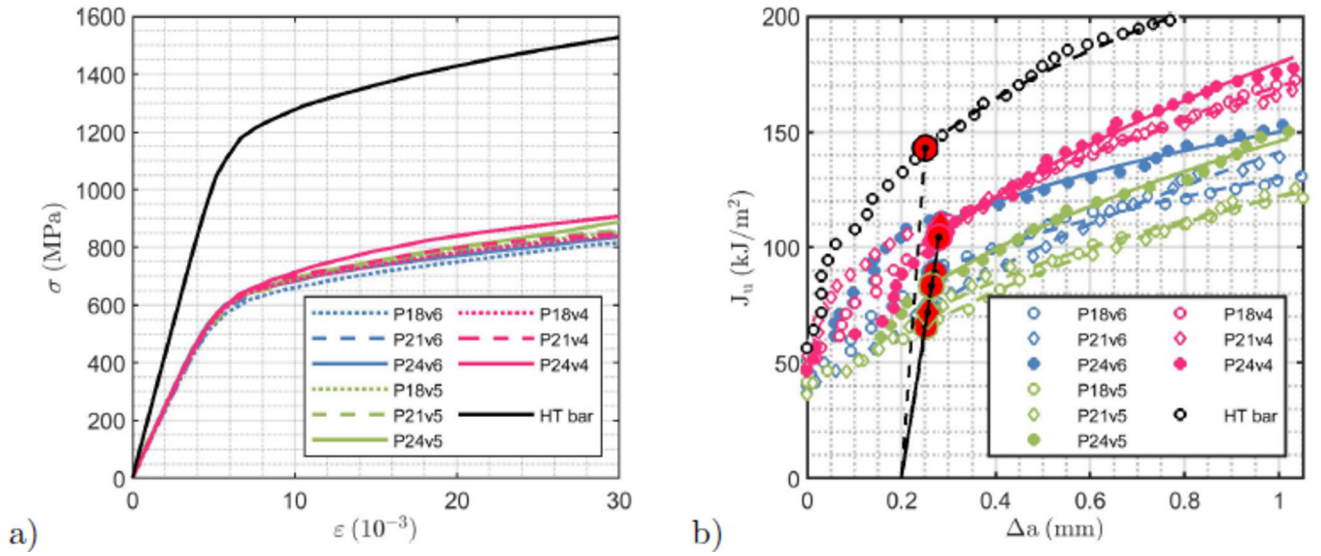

Fig. 7 Effect of process parameters on stress–strain behavior (a) and crack growth resistance curves (b)

speeds. Such a size difference may influence the yield strength, as described by Shi et al. (Ref 34) for a PBF-LB Al10SiMg alloy that featured a similar cellular microstructure. In our study, the relationship between the cellular microstructure and YS was not clearly identified (Fig. 5).

As observed by EBSD, the deposit texture systematically changed with the process parameters. The change can be documented by the histogram of grain boundary misorientation of the fiber clusters presented in Fig. 6(a). The specimens with slow scanning speeds exhibited a prominent and relatively narrow peak in the low-angle grain boundary (LAGB, $< 15^{\circ}$) range, indicating a cube texture. With the increasing scanning speed, the peak gradually loses its intensity and widens, eventually disappearing at the 60 m/min speed. Consequently, the density of high-angle grain boundaries (HAGB, $> 15^{\circ}$) increases, as could be seen from the calculated LAGB/HAGB ratio shown in Fig. 6(b). This clearly indicates a shift toward fiber texture, in line with the discussed change of the solidification mechanism. The observed presence of high-angle boundaries between the fiber clusters may promote solidification crack formation (Ref 21). Indeed, such cracks were found in the cross-sectional view (Fig. 5). They were located along the boundaries of the molten pool tracks, i.e., oriented in the LS plane. The number of cracks increased with increasing scanning speed and was accompanied by globular porosity chains. The corresponding porosities measured by image analysis were 0.04-0.02%,

Table 2 Effect of process parameters on linear energy density η, porosity Ψ, and mechanical and fracture properties

Material	η (kJ/m)	Ψ (%)	E (GPa)	YS (MPa)	ΔK_{th} (MPa$\sqrt{m}$)	ΔK_{thr} (MPa$\sqrt{m}$)	K_{IC} (MPa$\sqrt{m}$)
pl8v6	1.8	0.25±0.07	115	623	3.0	2.7	97.2
P21v6	2.1	0.91±0.63	113	647	4.2	3.8	87.8
p24v6	2.4	0.36±0.29	118	647	3.8	3.5	108.0
P18v5	2.16	0.35±0.20	119	649	3.7	3.4	83.5
P21v5	2.51	0.08±0.02	123	647	3.6	3.3	87.3
P24v5	2.88	0.16±0.12	118	648	3.4	3.1	94.1
pl8v4	2.7	0.04±0.00	116	650	3.9	3.5	106.4
P21v4	3.15	0.05±0.03	117	650	4.1	3.8	107.3
p24v4	3.6	0.04±0.02	119	663	3.7	3.4	105.2
HT bar			210	1222±52	7.72	6.27	148
HT bar	[49]	(R = 0.05)			7.75	6.33	...

The conventionally manufactured, wrought material tested in our study (HT bar) is provided as a reference, together with the same material tested in (Ref 49). The corresponding Paris coefficients of Hartmann–Schijve fit are $D = 2.58 \times 10^{-10}$ and $p = 2.19$ for the HS DED-LB deposits, and $D = 3.83 \times 10^{-11}$ and $p = 2.4$ for the two conventionally manufactured references

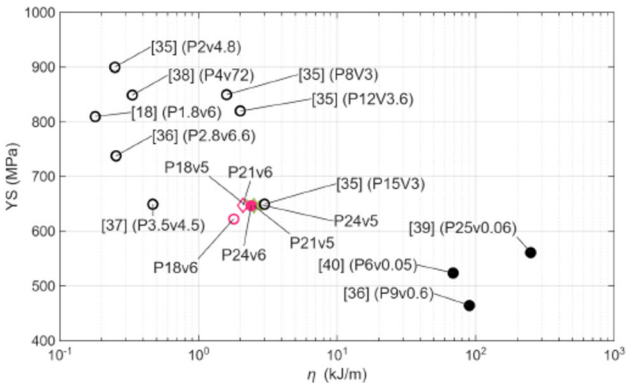

Fig. 8 Yield strength YS of investigated HS DED-LB deposits (colored data points) and reference fusion-based AM materials from (Ref 18, 35-40) (black circles: DED-LB full, PBF-LB empty), as a function of linear energy density η

0.18-0.15%, and 0.46-0.41% for the scanning velocities of 40, 50, and 60 m/min, respectively.

Stress–Strain Properties

The stress–strain curves were very similar for all tested process parameters (Fig. 7a), with the biggest difference recorded between the lowest and highest η samples, P18v6 and P24v4. This result suggests a rather robust character of the HS DED-LB method. As a result of the observed strong texture, the measured elastic moduli were significantly lower than those of the wrought reference material (Table 2). As no precipitation hardening was performed after the HS DED-LB deposition, the YS was also lower than the reference. It is important to note that none of the specimens fractured in the four-point bend test. This suggests that the ductility of the HS DED-LB Inconel 718 deposits exceeds $A > 5\%$, which is the limit of the method. In Fig. 8, the YS of the measured materials is shown as a function of linear energy density η along with available literature data. Low-η PBF-LB materials with finer grains show significantly higher YS than the high-η DED-LB. Our HS DED-LB deposits are positioned between these groups. One of the PBF-LB deposits studied in (Ref 35), a sample produced at high laser power and low scanning speed, resulted in η similar to our HS DED-LB deposits. Interestingly, this sample exhibited YS very similar to our materials.

Fracture Properties

Fatigue and fracture testing remains an almost underexplored topic in the literature regarding DED-LB (Ref 12). Indeed, only a few papers related to fatigue of PBF-LB or DED-LB of Inconel 718 exist (Ref 41-46).

The fracture properties measured in our study are represented by the quasi-static crack growth resistance curves shown in Fig. 7(b) and by the $\frac{da}{dN}$ versus ΔK curves shown in Fig. 9. The highest resistance was observed for the P24v4 sample, corresponding to the highest η. With increasing scanning speed, the resistance decreased. At every scanning speed, the highest crack resistance was always observed for the highest power, i.e., $P = 2.4$ kW.

The respective K_{IC} values calculated from the resistance curves were influenced by higher data noise in the low crack increments region. As such, the relationship between fracture toughness and the process parameters cannot be determined safely. Nevertheless, the values of $K_{IC} \sim 100$ MPa $\sqrt{m}$ obtained in our study are comparable to the results of as-built DED-LB and PBF-LB Inconel 718,

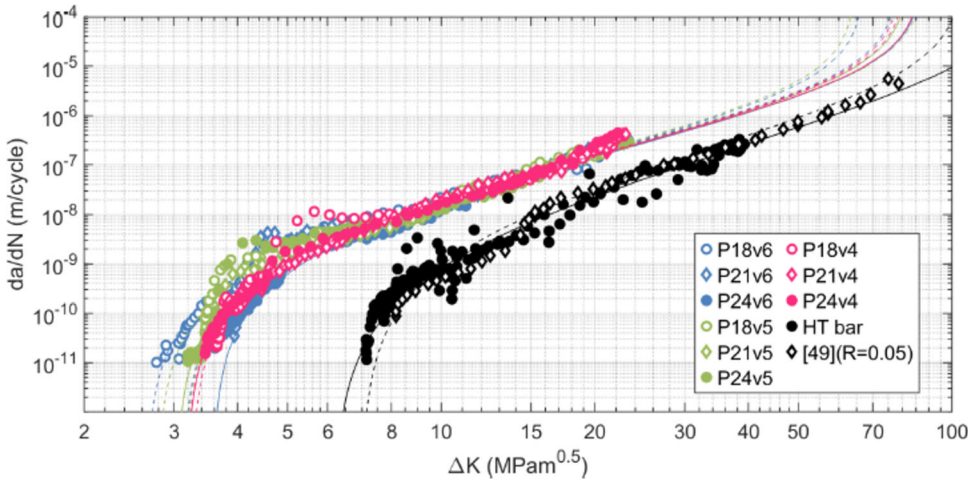

Fig. 9 Effect of process parameters on fatigue crack growth rate

reported as 86 MPa $\sqrt{m}$ and 110 MPa $\sqrt{m}$ in (Ref 17) and (Ref 47), respectively.

The fracture mechanical performance of the tested HS DED-LB and the wrought reference materials is summarized in Fig. 9 in the form of $\frac{da}{dN}$ curves and in Table 2 in the form of coefficients of the respective Hartmann–Schijve relation (Ref 48):

$$\frac{da}{dN} = D\left(\frac{\Delta K - \Delta K_{\text{thr}}}{\sqrt{1 - \frac{K_{\max}}{A}}}\right)^{p} \quad \text{(Eq 2)}$$

Here ΔK_{thr} is the fatigue crack growth rate threshold (note the difference to the threshold ΔK_{th} defined for $\frac{da}{dN} 0.17em= 10^{-10}$ m/cycle by ASTM E647), and the dynamic fracture toughness A was approximated by the measured fracture toughness K_{IC}. The $\frac{da}{dN}$ curves of the nine HS DED–LB deposits showed significant variability in the near-threshold region but converged at higher propagation rates beyond 10^{-9} m/cycle.

As expected, their fatigue crack growth resistance was inferior to those of the references in the entire ΔK range. Specifically, the fracture toughness K_{IC} and fatigue crack growth threshold ΔK_{thr} reached only about 50-70% and 40-65% of the reference values, respectively. The Paris coefficient D of the deposits was about 50% higher than that of the reference HT bars, again indicating a lower fracture performance. It should be recalled that in our experiments, we have adopted the $\Delta K = K_{\max}$ assumption recommended by the ASTM E647 standard. Therefore, the actual crack tip loading during the fatigue crack growth rate test corresponded to R 0 rather than the used remote stress ratio $R \sim 1$. This enabled us to compare our data with other low-R data commonly presented in the literature. Indeed, the comparison of the reference HT bar from our study with the $R = 0.05$ data tested by James in 1989 (Ref 49) yielded excellent agreement.

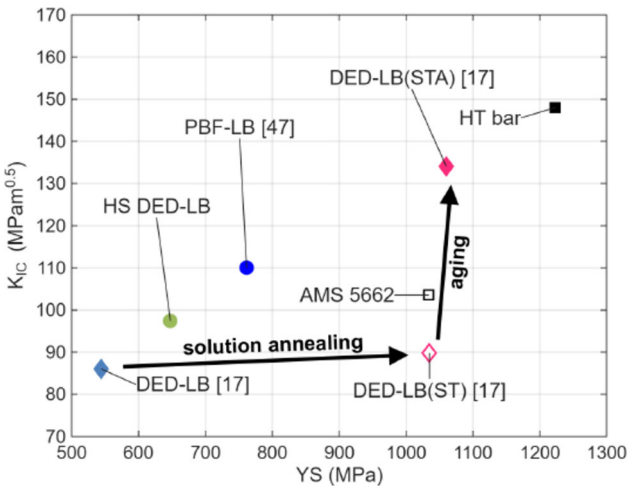

Fig. 10 Average fracture toughness K_{IC} and YS of the investigated HS DED-LB and reference Inconel 718 materials, compared with the AMS5562 requirements. DED-LB materials from (Ref 17) in as-built, solution treatment (ST), and solution-treated + aged (STA) state are included, along with the PBF-LB material in the as-built state from (Ref 47)

Comparing with the existing literature, our as-built HS DED-LB threshold values ΔK_{thr} were similar to those for the as-built (PBF-LB) Inconel 718 data obtained at η = 1 kJ/m by Konecna et al. in (Ref 41), reaching ΔK_{thr} = 3.0 MPa $\sqrt{m}$. Despite an expected significant improvement of the threshold values upon heat treatment, only slightly better values were reported for a heat-treated (DED-LB) Inconel 718 deposited at η = 50 kJ/m in (Ref 44), with ΔK_{thr} = 3.5 MPa $\sqrt{m}$. DED-LB Inconel 718 deposited at much higher η = 250 kJ/m in (Ref 39) reached ΔK_{thr} = 10.8 MPa $\sqrt{m}$ after solutionizing and precipitation hardening, outperforming the conventionally manufactured material. The next study planned by our group will

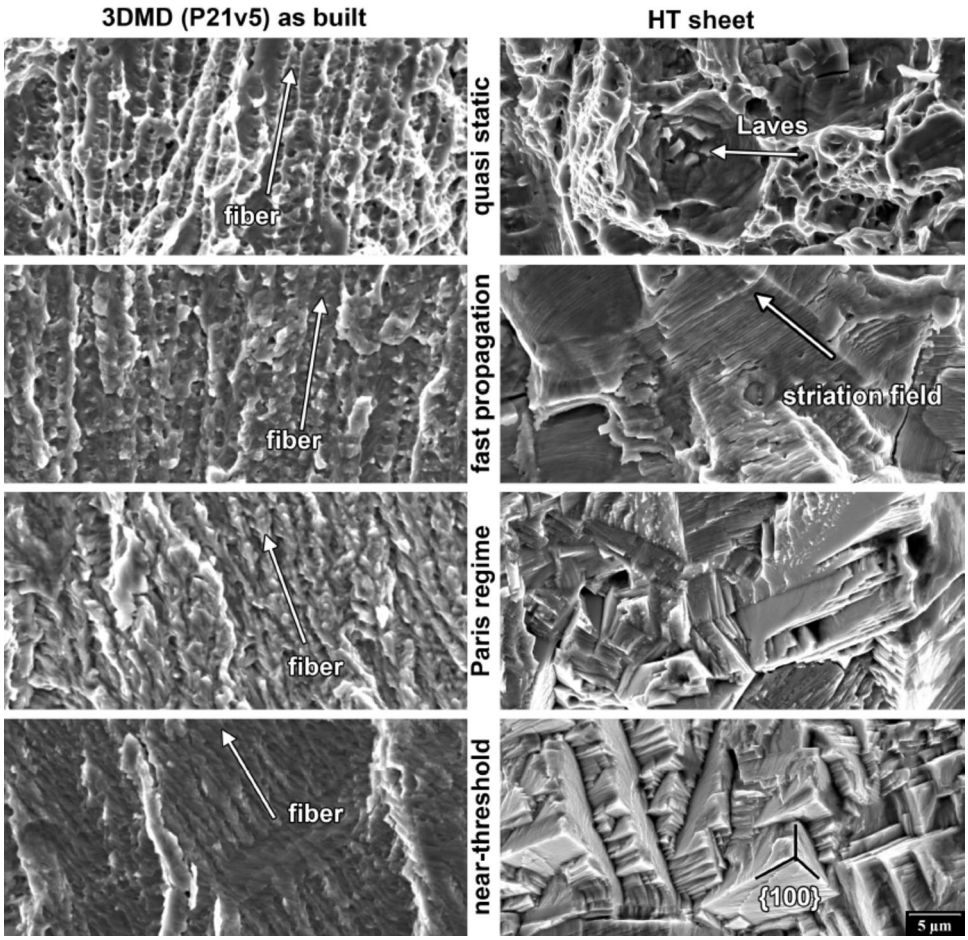

Fig. 11 Typical fracture surfaces of the near threshold, Paris, fast fatigue propagation, and the final quasi-static fracture regions compared to the reference HT bar. Specimen P21v5 shown

therefore focus on this aspect by testing the low η HS DED-LB materials in their precipitation-hardened state.

The tested HS DED-LB materials can also be compared with the literature data in terms of the K_{IC} to YS relation (Fig. 10). The DED-LB materials from (Ref 17) tested in the as-built, solution annealed, and solution annealed + aged states clearly illustrate the positive effect of solution annealing on YS and the increase in fracture toughness after aging. Materials formed by PBF-LB from (Ref 47) in the as-built state are also included for comparison to represent a method with significantly lower η. As already observed in Fig. 8, the HS DED-LB material in the as-built state outperforms the DED-LB but shows lower YS than the PBF-LB material.

Fracture Mechanisms

The macroscopic images of the fracture surfaces are shown in Fig. 5, while details corresponding to different crack propagation stages are shown in Fig. 11. As all the HS DED-LB deposits showed similar fracture morphology, only one specimen is presented (P21v5, deposited at moderate parameter values). The fatigue fracture in the near-threshold region was very flat and transgranular, following the <100> directions of the crystal fibers. The effects of texture, porosity, and the existence of solidification cracks influenced the variability of crack propagation in this near-threshold range. Significantly coarser crystallographic fracture was observed for the reference HT bar due to its coarse microstructure.

In the Paris regime, the fracture surfaces became rougher for both the HS DED-LB deposit and the reference HT bar. This could be attributed to the activation of additional slip planes contributing to the crack growth. Therefore, the effect of texture and porosity of the HS DED-LB deposits was lower than in the near-threshold range, as the cracks were able to deflect more easily. Fatigue striations were observed at higher crack propagation rates for the reference material, but were not apparent in the HS DED-LB samples.

At quasi-static load, fiber decohesion characterized by small ductile dimples was observed in the HS DED-LB deposits. The reference HT bar material fractured, creating ductile dimples typical of quasi-static fracture in Inconel 718. The number of solidification cracks increased with the scanning speed (Fig. 5). These solidification cracks were oriented in parallel to the loading direction. Therefore, their effect on

the measured mechanical and fracture properties was small. A much higher effect of solidification cracks could be expected for specimens loaded in the T direction, i.e., for T-S and T-L orientations, planned by our group in the near future.

Conclusions

The performed testing and characterization provided unique material data for the HS DED-LB deposits of Inconel 718 obtained at linear energy density η range specific for ultra-high deposition speeds. This η range complements the currently available data for other fusion-based AM methods, namely it fills the gap between PBF-LB and DED-LB with lower and higher η, respectively. It was shown that by varying the process parameters, the material texture can be tuned from fiber texture at low η to cube texture at high η. At the low η, the occurrence of high-angle boundaries in the fiber texture correlated with the formation of solidification cracks. Surprisingly, despite the strong influence of the process parameters on microstructure, their effect on mechanical and fracture properties was relatively small in the as-built state. This indicates the exceptional robustness of the method for applications where subsequent heat treatment is either complicated or cannot be performed at all, typically for repairs. Nevertheless, a post-print heat treatment could significantly enhance the mechanical and fracture properties, either preserving or modifying the as-deposited texture. The follow-up study will therefore focus on the optimization of subsequent solutionizing and precipitation-hardening heat treatments to investigate whether the mechanical and fracture properties of HS DED-LB Inconel 718 can be brought to levels comparable with directionally solidified materials or materials with equiaxed grain structure.

Acknowledgments The project FerrMion of the Ministry of Education, Youth, and Sports, Czech Republic, co-funded by the European Union (CZ.02.01.01/00/22_008/0004591) and the project of the Grant Agency of the Czech Technical University (SGS24/147/OHK4/3T/14SGS) are gratefully acknowledged. A.A. and J.C. acknowledge the funding from the European Union's Horizon Europe research and innovation programme under the Marie Skłodowska-Curie grant agreement No. 101119988 (REMAKE). The authors acknowledge the use of the facilities at the Chair of Digital Additive Production (DAP), Faculty of Mechanical Engineering, RWTH Aachen University, Aachen, Germany, for the deposition of the specimens.

Funding Open access publishing supported by the institutions participating in the CzechELib Transformative Agreement.

References

1. M. Perrut, P. Caron, M. Thomas, and A. Couret, High Temperature Materials for Aerospace Applications: Ni-Based Superalloys and γ-TiAl Alloys, *C. R. Phys.*, 2018, **19**(8), p 657–671.
2. R. Ortiz-Fernandez, and B. Jodoin, Toward Efficient Cold Spraying of Inconel 718: Understanding the Influence of Coating and Particle Impact Temperatures, *J. Therm. Spray Technol.*, 2022, **32**(1), p 188–207.
3. M. Balbaa, S. Mekhiel, M. Elbestawi, and J. McIsaac, On Selective Laser Melting of Inconel 718: Densification, Surface Roughness, and Residual Stresses, *Mater. Des.*, 2020, **193**, p 108818.
4. F. Brenne, A. Taube, M. Pröbstle, S. Neumeier, D. Schwarze, M. Schaper, and T. Niendorf, Microstructural Design of Ni-Base Alloys for High-Temperature Applications: Impact of Heat Treatment on Microstructure and Mechanical Properties After Selective Laser Melting, *Prog. Addit. Manuf.*, 2016, **1**(3–4), p 141–151.
5. M. Valdez, C. Kozuch, E.J. Faierson, and I. Jasiuk, Induced Porosity in Super Alloy 718 Through the Laser Additive Manufacturing Process: Microstructure and Mechanical Properties, *J. Alloys Compd.*, 2017, **725**, p 757–764.
6. M. Bambach, I. Sizova, F. Kies, and C. Haase, Directed Energy Deposition of Inconel 718 Powder, Cold and Hot Wire Using a Six-Beam Direct Diode Laser Set-Up, *Addit. Manuf.*, 2021, **47**, p 102269.
7. M. Bambach, I. Sizova, F. Silze, and M. Schnick, Comparison of Laser Metal Deposition of Inconel 718 from Powder, Hot and Cold Wire, *Procedia CIRP*, 2018, **74**, p 206–209.
8. A.S. Johnson, S. Shao, N. Shamsaei, S.M. Thompson, and L. Bian, Microstructure, Fatigue Behavior, and Failure Mechanisms of Direct Laser-Deposited Inconel 718, *JOM*, 2016, **69**(3), p 597–603.
9. S. Sreekanth, E. Ghassemali, K. Hurtig, S. Joshi, and J. Andersson, Effect of Direct Energy Deposition Process Parameters on Single-Track Deposits of Alloy 718, *Metals*, 2020, **10**(1), p 96.
10. L.L. Parimi, G.A. Ravi, D. Clark, and M.M. Attallah, Microstructural and Texture Development in Direct Laser Fabricated in 718, *Mater Charact*, 2014, **89**, p 102–111.
11. Q.-l. Zhang, J.-H. Yao, and J. Mazumder, Laser Direct Metal Deposition Technology and Microstructure and Composition Segregation of Inconel 718 Superalloy, *J. Iron. Steel Res. Int.*, 2011, **18**(4), p 73–78.
12. T.R.F. Cavalcante, F.E. Mariani, and J.A.A. Diaz, Additive Manufacturing of Inconel 718: A Review on Microstructures and Mechanical Prop-erties of Ded-lb-Processed Samples, *J. Mater. Res.*, 2025 https://doi.org/10.1557/s43578-025-01663-y

13. C. Kumara, D. Deng, J. Moverare, and P. Nylén, Modelling of Anisotropic Elastic Properties in Alloy 718 Built by Electron Beam Melting, *Mater. Sci. Technol.*, 2018, **34**(5), p 529–537.
14. M. Shahwaz, P. Nath, and I. Sen, A Critical Review on the Microstructure and Mechanical Properties Correlation of Additively Manufactured Nickel-Based Superalloys, *J. Alloy. Compd.*, 2022, **907**, p 164530.
15. Y. Zhao, Q. Guo, D. Zunfeng, S. Chen, J. Tan, Z. Yang, and Z. Ma, Critical Role of Subgrain Orientation on the Stability of Mechanical Properties of Selective Laser Melting Manufactured Alloys, *Mater. Sci. Eng. A*, 2022, **832**, p 142505.
16. M.J. Donachie and S.J. Donachie, *Superalloys: A Technical Guide*, ASM International, 2002.
17. Y. Xiaobin, X. Lin, F. Liu, L. Wang, Y. Tang, J. Li, S. Zhang, and W. Huang, Influence of Post-Heat-Treatment on the Microstructure and Fracture Toughness Properties of Inconel 718 Fabricated with Laser Directed Energy Deposition Additive Manufacturing, *Mater. Sci. Eng. A*, 2020, **798**, p 140092.
18. S. Heo, Y. Lim, N. Kwak, C. Jeon, M. Choi, and I. Jo, Impact of Heat Treatment and Building Direction on Tensile Properties and Fracture Mechanism of Inconel 718 Produced by Slm Process, *Metals*, 2024, **14**(4), p 440.
19. X.G. Yang, B. Li, M.L. Wang, S.Q. Guo, G.L. Miao, D.Q. Shi, and Y.S. Fan, Correlation Between Microstructures and Mechanical Properties of a Slm Ni-Based Superalloy After Different Post Processes, *J. Market. Res.*, 2024, **32**, p 955–966.
20. X. Zhang, M. Ya-hang, L. Ma, J.-J. Liang, Y.-Z. Zhou, X.-F. Sun, and J.-G. Li, Cracking on a Nickel-Based Superalloy Fabricated by Direct Energy Deposition, *China Foundry*, 2024, **21**(4), p 311–318.
21. A. Ramakrishnan and G.P. Dinda, Direct Laser Metal Deposition of Inconel 738, *Mater. Sci. Eng. A*, 2019, **740–741**, p 1–13.
22. J. Schaible, L. Sayk, T. Schopphoven, J.H. Schleifenbaum, and C. Häfner, Development of a High-Speed Laser Material Deposition Process for Additive Manufacturing, *J. Laser Appl.*, 2020 https://doi.org/10.2351/7.0000320
23. S. Maffia, O. Kovarik, J. Cech, and T. Stittgen, Investigating the application of 3d-ehla for microstructure control in large-scale additive manufacturing. In *Euro PM2024 Proceedings*, 2024
24. ASTM E399-09, *Standard Test Method for Linear-Elastic Plane-Strain Fracture Toughness K_{IC} of metallic materials*. West Conshohocken, PA, 2009
25. J. Čížek, O. Kovářík, J. Cupera, J. Kondas, T. Bajer, F. Siska, M. Janovska, and H. Seiner, Measurement of Mechanical and Fatigue Properties Using Unified, Simple-Geometry Specimens: Cold Spray Additively Manufactured Pure Metals, *Surf. Coat. Technol.*, 2021 https://doi.org/10.1016/j.surfcoat.2021.126929
26. J. Blaber, B. Adair, and A. Antoniou, Ncorr: Open-Source 2D Digital Image Correlation Matlab Software, *Exp. Mech.*, 2015, **55**(6), p 1105–1122.
27. H. Herbert, Ueber den Zusammenhang der Biegungselastizität des Gußeisens mit seiner Zug- und Druckelastizität. *Forschungsarbeiten auf dem Gebiete des Ingenieurwesens*, p. 39–81, (1910)
28. O. Kovářík, A. Janca, and J. Siegl, Fatigue Crack Growth Rate in Miniature Specimens Using Resonance, *Int. J. Fatigue*, 2017, **102**, p 252–260. (**cited By 9**)
29. O. Kovářík, A. Materna, J. Siegl, J. Čížek, and J. Klecka, Fatigue Crack Growth in Plasma-Sprayed Refractory Materials, *J. Therm. Spray Technol.*, 2019, **28**(1–2), p 87–97.
30. ASTM E647-15e1, *Standard Test Method for Measurement of Fatigue Crack Growth Rates*. (ASTM International, West Conshohocken, PA, 2015)
31. E1820-18ae12019, *Standard Test Method for Measurement of Fracture Toughness*. (ASTM International, West Conshohocken, PA, 2019)
32. R. Jiang, Z. Ren, J. Aroh, A. Mostafaei, B. Gould, T. Sun, and A.D. Rollett, Quantifying Equiaxed vs Epitaxial Solidification in Laser Melting of Cmsx-4 Single Crystal Superalloy, *Metall. and Mater. Trans. A.*, 2022, **54**(3), p 808–822.
33. G.P. Dinda, A.K. Dasgupta, and J. Mazumder, Texture Control During Laser Deposition of Nickel-Based Superalloy, *Scripta Mater.*, 2012, **67**(5), p 503–506.
34. S. Shi, Y. Zhao, X. Lin, H. Deng, L. Zhao, G. He, and W.-D. Huang, Significance of α-Al Cellular Matrix in Tensile Behavior and Work-Hardening of Additive Manufactured AlSi10Mg Alloy, *Virtual Phys. Prototyp.*, 2025 https://doi.org/10.1080/17452759.2024.2449189
35. H. Yang, Z. Wang, H. Wang, Y. Wu, and H. Wang, Microstructure, Mechanical Property and Heat Treatment Schedule of the Inconel 718 Manufactured by Low and High Power Laser Powder Bed Fusion, *Mater. Sci. Eng. A*, 2023, **863**, p 144517.
36. G. Meng, Y. Gong, J. Zhang, Z. Jiang, Q. Ren, and J. Zhao, Microstructure and Mechanical Properties of Inconel 718 Thin Walls Prepared by Laser Direct Energy Deposition and Selective Laser Melting, *Thin-Walled Struct.*, 2023, **193**, p 111284.
37. Ü.G. Başcı, E. Avcu, M. Kıraç, A. Sever, İ Gökalp, H.-M. Yavuz, S. Oktay, E. Abakay, Y.Y. Avcu, and R. Yamanoğlu, Microstructural, Mechanical, and Tribological Properties of Selective Laser Melted Inconel 718 Alloy: The Influences of Heat Treatment, *Crystals*, 2024, **15**(1), p 18.
38. D. Zhang, W. Niu, X. Cao, and Z. Liu, Effect of Standard Heat Treatment on the Microstructure and Mechanical Properties of Selective Laser Melting Manufactured Inconel 718 Superalloy, *Mater. Sci. Eng. A*, 2015, **644**, p 32–40.
39. X. Yu, X. Lin, H. Tan, Y. Hu, S. Zhang, F. Liu, H. Yang, and W. Huang, Microstructure and Fatigue Crack Growth Behavior of Inconel 718 Super-Alloy Manufactured by Laser Directed Energy Deposition, *Int. J. Fatigue*, 2021, **143**, p 106005.
40. I. Miguel, G. Artola, J.I. Arrizubieta, A.I. Fernández-Calvo, and C. Angulo, Inconel 718 Hybrid Laser-Based Directed Energy Deposition and Wrought Component Characterization Through Small Punch Tests, *Appl. Sci.*, 2024, **14**(15), p 6420.
41. R. Konečná, L. Kunz, G. Nicoletto, and A. Bača, Long Fatigue Crack Growth in Inconel 718 Produced by Selective Laser Melting, *Int. J. Fatigue*, 2016, **92**, p 499–506.
42. I. Černý, J. Kec, A. Poloch, and M. Zetek, Mechanical properties and high-cycle fatigue strength of 3d printed inconel 718 alloy and effects of high-temperature ex-posure to corrosive atmosphere. In *FRACTURE AND DAMAGE MECHANICS: Theory, Simulation and Experiment*, **2309**, p. 020026. AIP Publishing, 2020
43. X Yu, X Lin, F Liu, Y Hu, S Zhang, Y Zhan, H Yang, and W Huang, Microstructure and Fatigue Crack Growth Behavior OF Inconel 718 Superalloy Fabricated via Laser Directed Energy Deposition Additive Manufacturing. SSRN Electr. J., (2020)
44. M. Rashkovets, N. Kislov, M. Gushchina, A. Nikulina, A. Popelukh, and O. Klimova-Korsmik, Phase Composition and Fatigue Crack Growth Behavior of Inconel 718 Under Additive Manufacturing, *Mater. Sci. Eng. A*, 2022, **851**, p 143595.
45. R. Ghiaasiaan, A. Poudel, N. Ahmad, P.R. Gradl, S. Shao, and N. Shamsaei, High Temperature Tensile and Fatigue Behaviors of Additively Manufactured In625 and In718, *Procedia Struct. Integr.*, 2022, **38**, p 581–587.
46. P.D. Nezhadfar, A.S. Johnson, and N. Shamsaei, Fatigue Behavior and Microstructural Evolution of Additively Manufactured Inconel 718 Under Cyclic Loading at Elevated Temperature, *Int. J. Fatigue*, 2020, **136**, p 105598.
47. M. Seifi, A. A. Salem, D. P. Satko, R. Grylls, and J. J. Lewandowski. *Effects of Post-processing on Microstructure*

and Mechanical Properties of SLM-Processed IN-718, p. 515–526. Springer International Publishing, 2018
48. K.-H. Schwalbe, S. Kalluri, R.M. McGaw, A. Neimitz, and S.W. Dean, On the Beauty of Analytical Models for Fatigue Crack Propagation and Fracture—A Personal Historical Review, *J. ASTM Int.*, 2010, **7**(8), p 102713.
49. L.A. James, Fatigue Crack Propagation in Alloy 718: A Review. Superalloys, p. 499–515 (1989)